Published in "Physical Review A 75(2): 022512, 2007"
which should be cited to refer to this work.

High-resolution study of the x-ray resonant Raman scattering process around the 1*s* absorption edge for aluminium, silicon, and their oxides

J. Szlachetko,* J.-Cl. Dousse, M. Berset, K. Fennane, and M. Szlachetko
Department of Physics, University of Fribourg, CH-1700 Fribourg, Switzerland

J. Hoszowska† and R. Barrett
European Synchrotron Radiation Facility (ESRF), F-38043 Grenoble, France

M. Pajek and A. Kubala-Kukus
Swietokrzyska Academy, Institute of Physics, 25-406 Kielce, Poland

X-ray resonant Raman scattering (RRS) spectra of Al, Al_2O_3, Si, and SiO_2 were measured at the European Synchrotron Radiation Facility, using a high-resolution Bragg-type curved crystal spectrometer. The x-ray RRS spectra were collected at several beam energies tuned below the 1*s* absorption thresholds of Al and Si. Differences in the spectral features between the elemental samples and the oxide ones were clearly observed. The data were interpreted using the second-order perturbation theory within the Kramers-Heisenberg (KH) approach. It is shown that, using the KH formalism, oscillator strengths that are similar to the ones deduced from x-ray absorption measurements can be extracted from emission x-ray RRS spectra. The total cross sections for the x-ray RRS process were derived for the different photon beam energies and compared with theoretical predictions. For elemental silicon, the weak 1*s*-3*p* excitation was observed and found to be consistent with results of density of states calculations.

I. INTRODUCTION

Intense, monoenergetic, and energy-tunable x-ray sources have become a very important tool in material sciences, in particular for the investigation of electronic states and electron-electron correlations in insulators, semiconductors, and metals. Synchrotron radiation has played a major role in this development, being extensively used for state-selective studies in both x-ray absorption spectroscopy (XAS) and x-ray photoelectron spectroscopy (XPS). X-ray emission spectroscopy (XES) and resonant inelastic x-ray scattering (RIXS) represent alternative techniques to probe electronic excitations in condensed matter systems [1]. However, due to the small signals of XES and RIXS which are spectroscopies of second order optical processes, very intense x-ray sources are needed to obtain precise experimental data. In this respect, a tremendous development of XES and RIXS studies has occurred in the last decade due to the advent of high-brilliance x-ray sources offered by third-generation synchrotron radiation facilities.

Like RIXS, x-ray Raman scattering is a photon-in and photon-out second-order process. In this process a core electron is excited into a bound state just above the Fermi level by absorption of a photon. The intermediate virtual state then decays radiatively, the initial core hole being filled by another inner-shell electron with simultaneous emission of a photon. The energy of the inelastically scattered photon is equal to the energy of the incoming photon minus the sum of the binding energy of the inner-shell hole in the final state and energy above the Fermi level of the excited core electron. In comparison with first-order processes, x-ray Raman scattering intensities are much weaker except if the energy of the incoming photon is close to an absorption threshold. In this case, the Raman process is resonantly enhanced and its cross section increases drastically. The x-ray resonant Raman scattering (RRS) process can be regarded as a particular case of RIXS in which the scattered photons are characterized by discrete final states [2]. Pioneering works on x-ray RRS were performed in the seventies using x-ray tubes [3] and synchrotron radiation [4].

X-ray RRS has been used extensively in the last years to study the electronic structure of numerous elements and compounds [1]. Up to now, most studies were carried out for transition metals [5–7] and rare-earth-metal elements [8,9] whereas, for low-*Z* elements, x-ray RRS information is more scarce [10–12]. For silicon, data were collected mostly about the $L_{2,3}$ edges [13,14] and more rarely at the *K* edge [15]. In these experiments, it was shown that the x-ray RRS emission spectra exhibit features which can be used to study the valence and conduction bands. In particular, the shapes of the Si x-ray RRS spectra observed at the L_3 edge were found to be well reproduced by band-structure calculations [16]. In contrast to that, to our knowledge no x-ray RRS study around *K*-edge has been reported so far for Al, nor for Al_2O_3. This is somewhat surprising because novel aluminium based materials [17] and aluminium oxides [18], which are widely used in industrial applications, have been intensively investigated using other methods.

*On leave from Swietokrzyska Academy, Institute of Physics, 25-406 Kielce, Poland.
†Present address: Department of Physics, University of Fribourg, CH-1700 Fribourg, Switzerland.

The x-ray RRS process also plays an important role in the determination of light element impurities on the surface of ultra clean substrates by means of the total reflection x-ray fluorescence (TXRF) method [19]. The TXRF method is affected by the x-ray RRS process because the latter represents an important source of background. For instance, recent experiments have shown [20,21] that the detection threshold of Al impurities on the surface of ultra pure silicon wafers is limited by the presence of RRS x-rays. For incident photon energies tuned below the Si 1*s* absorption edge to avoid the intense Si $K\alpha$ fluorescence peak, the broad x-ray RRS spectrum of Si is indeed overlapping with the Al $K\alpha$ fluorescence line. Detailed knowledge of the shape and yield of the Si x-ray RRS spectrum is therefore crucial for optimization of the measuring parameters and also assessing the practical minimum detection limits for light element impurities which can be attained. Up to now, due to the lack of existing experimental data, only theoretical predictions [1,22–24] have been used for the determination of the x-ray RRS background in ultra pure silicon wafers. However, the sensitivity of the TXRF method being limited by the uncertainties related to these calculations, an experimental verification of the theoretical predictions is highly desirable.

In this paper, we report on high-resolution measurements of the x-ray RRS spectra of Al, Si, Al_2O_3, and SiO_2. Partial results concerning elemental silicon were already published in [25]. The spectra were collected at several incident photon energies below the *K*-edges of Al and Si. The shapes of the observed x-ray RRS spectra were compared to predictions based on the Kramers-Heisenberg theory. They were found to be well reproduced by the calculations over wide ranges of beam energy, provided that proper oscillator strength distributions are used. Using the equations proposed by Tulkki and Åberg [22], we were able to extract for all samples the oscillator strength distributions from the corresponding experimental x-ray RRS spectra. The obtained distributions were found to exhibit similar shapes and features as the curves measured by means of the near edge absorption technique. The absolute x-ray RRS cross sections and their variation with the beam energy were determined for the four samples. For elemental silicon, for which data were also taken using beam energies tuned across the *K* edge, the weak 1*s*-3*p* excitation could be observed for the first time and its cross section determined.

II. EXPERIMENT

The measurements were performed at the European Synchrotron Radiation Facility (ESRF), in Grenoble, France. The x-ray RRS spectra were measured by means of high-resolution, using a Bragg type von Hamos bent crystal spectrometer [26], installed at the beam line ID21, downstream from the chamber of the scanning transmission x-ray microscope. The spectrometer was equipped with a 10 cm high $\times$5 cm wide$\times$0.03 cm thick (101) ADP (Ammonium Dihydrogen Phosphate) crystal (2d=10.642 Å), curved cylindrically to a radius of 25.4 cm. The x-ray source width, which is crucial for the resolving power of the spectrometer, was defined by a narrow rectangular slit, consisting of two juxtaposed vertical 0.3 mm thick Ta plates, placed between the crystal and the target. By decreasing the slit width the resolution of the spectrometer is improved but its efficiency diminishes. To satisfy at best the conditions of this experiment a slit width of 0.2 mm was chosen. The x rays diffracted by the crystal were recorded with a position-sensitive back illuminated CCD (charge coupled device) detector consisting of 1340 columns and 400 rows with a pixel size of 20 $\times$20 μm^2. In order to reduce the dark current noise the CCD chip was thermoelectrically cooled down to −50 °C. The energy calibration of the von Hamos spectrometer was determined by measuring the fluorescence $K\alpha$ lines of Al and Si at incident photon energies 50 eV above the *K* edges of the two elements. These measurements were also used to determine the response function of the spectrometer. The latter was found to be well reproduced by a Gaussian profile with a full width at half maximum (FWHM) of 0.8 eV for Al and 0.9 eV for Si.

The white beam delivered by the ID21 undulator was monochromatized by means of two 20 Å Ni/B_4C multilayers. Higher-energy photons were rejected with an efficiency better than 99.9% by means of a Ni mirror. Depending on the energy, 10^{10}–10^{11} incident photons per second with a FWHM energy resolution of about 6 eV were obtained on the samples, which represented a good compromise between a high enough beam intensity to observe the weak x-ray RRS spectra and an acceptable beam energy resolution. The monochromator was calibrated in energy by measuring the Al and Si *K*-absorption edges in the fluorescence mode using a Si(Li) detector.

Solid targets of metallic Al, polycrystalline Si, and amorphous Al_2O_3 and SiO_2 with a thickness of 1 mm were employed. Purities of the samples were 99.999% for Al and Si, 97.5% for Al_2O_3, and 99.9% for SiO_2. The spot size of the beam on the target was about 1 mm in diameter. For each sample, the angle between the beam and the target surface was set to 20 degrees. Test-measurements performed at smaller incident angles to better reproduce the experimental conditions of low resolution TXRF measurements that are carried out at grazing incidence angles showed x-ray RRS yields too poor to be measured in reasonable collecting times by means of high resolution.

The x-ray RRS data were recorded in the energy range between 1400 eV and 1490 eV for Al and Al_2O_3, and between 1640 eV and 1760 eV for Si and SiO_2. The CCD size along the dispersion axis (26.8 mm) permitted us to cover an energy range of about 40 eV. Thus two to three CCD lengths were required to observe the x-ray RRS spectra of interest. Data were acquired in the so-called multiple frame mode. Numbers of collected images for single measurements varied between 200 and 600 with exposure times of 1 s to 10 s per image. Exposure times were chosen depending on the photon intensity on the CCD in order to avoid multiple hits on single pixels. The CCD camera was operated through a dedicated controller at a rate of 1 MHz so that the time needed to read each two-dimensional image amounted to about 0.5 s. To reject higher order reflection events and diminish the background the acquired images were filtered online by setting

suitable energy windows on the CCD. The sum of all filtered images was then projected onto the dispersion axis giving the energy spectrum.

III. THEORY

X-ray RRS differential cross sections can be determined using the formulas developed by Tulkki and Åberg [22,23] within the Kramers-Heisenberg model. In the present study the x-ray RRS process consists of the excitation of a $1s$ core electron into an intermediate unoccupied level. This "virtual" state then decays radiatively by a $2p \rightarrow 1s$ transition as schematically shown in Fig. 1(a). As reported by Åberg and Tulkki [23], the anisotropic interference term between the resonant and nonresonant amplitudes becomes very small close to the K edge. Assuming therefore this term to be negligible in our case, the x-ray RRS differential cross section can be written as follows:

$$\frac{d\sigma(\omega_1)}{d\omega_2} = A \int_0^\infty \frac{\omega_2}{\omega_1} \frac{(\omega_{1s} - \omega_{2p_j}) g_{2p_j} (\omega_{1s} + \omega)(dg_{1s}/d\omega)}{(\omega_{1s} + \omega - \omega_1)^2 + \Gamma_{1s}^2/4\hbar^2} \times \frac{\Gamma_{2p_j}/2}{(\omega_1 - \omega_{2p_j} - \omega - \omega_2)^2 + \Gamma_{2p_j}^2/4\hbar^2} d\omega, \qquad (1)$$

where A is a normalization constant, $\hbar\omega_1$ and $\hbar\omega_2$ are the energies of the incoming and outgoing photons and $\hbar\omega$ stands for the energy above the Fermi level of the excited electron. The oscillator strength for the $2p \rightarrow 1s$ transition is represented by g_{2p_j}, where $j = 1/2$ or $3/2$, depending on whether the final vacancy is located in the L_2 or L_3 subshell. The $dg_{1s}/d\omega$ represents the oscillator strength distribution for $1s$ absorption. It is a function of the excited electron energy. The second term in Eq. (1) represents the normalized final state density function that accounts for the final state broadening (Γ_{2p_j}) and ensures the energy conservation which is given by:

$$\hbar\omega_2 = \hbar\omega_1 - \hbar\omega_{2p_j} - \hbar\omega. \qquad (2)$$

As an example the theoretical x-ray RRS profile given by Eq. (1) is shown in Fig. 1(b). Calculations were performed for Si assuming an ideally monochromatic beam having an energy of 1820 eV, i.e., an energy 20 eV below the $1s$ threshold. The binding energies $\hbar\omega_{1s}$ and $\hbar\omega_{2p}$, the atomic level widths Γ_{1s}, Γ_{2p_j} and the oscillator strength g_{2p_j} were taken from [27–29], respectively. To simplify the calculations, a step function was assumed for the oscillator strength distribution $dg_{1s}/d\omega$ [see inset in Fig. 1(b)].

As it can be seen from Fig. 1(b) the x-ray RRS profile presents a long low-energy tail which is due to the Lorentzian shape of the involved $1s$ atomic level. At the low energy limit ($\hbar\omega_2 \rightarrow 0$) the differential cross section $d\sigma(\omega_1)/d\omega_2$ vanishes. The sharp high-energy cut-off is defined by the energy conservation [$\hbar\omega = 0$ in Eq. (2)] and moves toward lower energies when the energy of the incoming photons decreases.

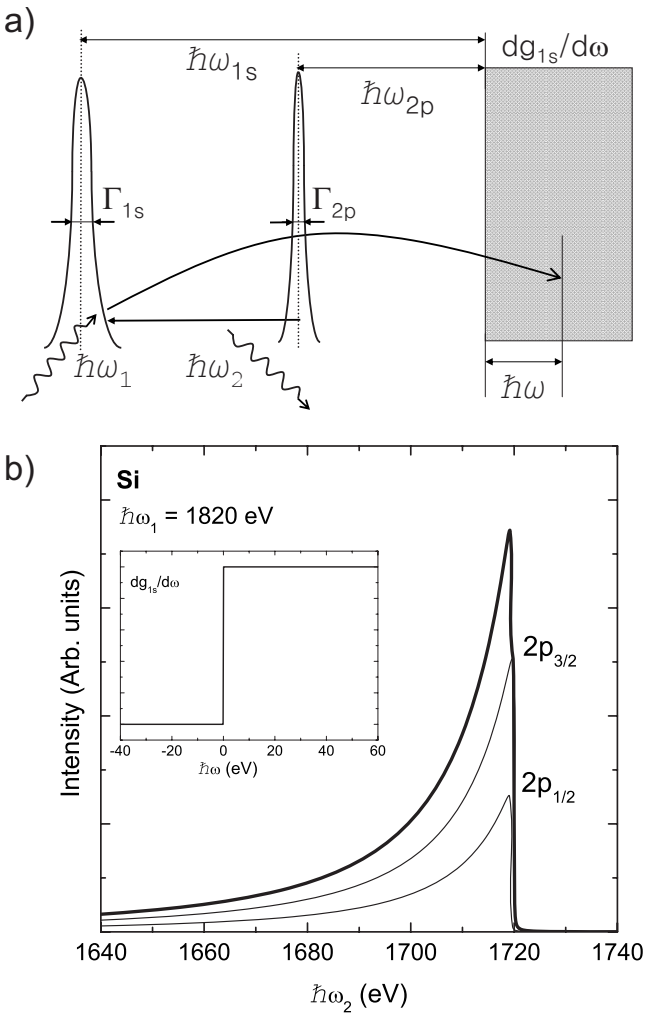

FIG. 1. (a) Energy diagram of the x-ray RRS process involving $1s$ and $2p$ electrons. (b) Theoretical Si x-ray RRS profiles assuming the final vacancy in the L_2 or L_3 subshell (thin solid lines) and their sum (thick solid line). Calculations were done for incoming photons with an energy 20 eV below the K edge. The inset shows the simple step function model used in the calculations for the oscillator strength distribution $dg_{1s}/d\omega$.

Due to the choice of a step function for the oscillator strength distribution, the theoretical x-ray RRS profile presented in Fig. 1(b) does not show any fine structures. Actually, a more realistic $dg_{1s}/d\omega$ distribution would contain peaks and oscillations similar to those observed in x-ray absorption fine structure (XAFS) spectra. These fine structures should then be reflected in the measured x-ray RRS spectra because in the Raman process by exciting $1s$ electrons above the Fermi level one scans the density of unoccupied bound states in the atom. As a consequence, realistic $dg_{1s}/d\omega$ distributions should be deducible from experimental x-ray RRS spectra.

In order to calculate analytically the $dg_{1s}/d\omega$, the normalized density function in Eq. (1) can be replaced by the Dirac delta function [23,30], provided that the width of the final state is negligibly small. Indeed, within this approximation Eq. (1) can be expressed as

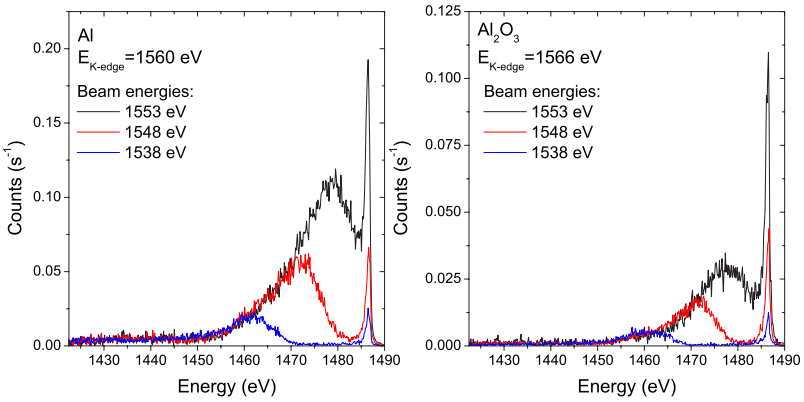

FIG. 2. (Color online) High-resolution x-ray RRS spectra of Al and Al_2O_3 measured for different beam energies tuned below the $1s$ absorption edge.

$$\frac{d\sigma(\omega_1)}{d\omega_2} = A\int_0^\infty \frac{\omega_2}{\omega_1}\frac{(\omega_{1s}-\omega_{2p_j})g_{2p_j}(\omega_{1s}+\omega)(dg_{1s}/d\omega)}{(\omega_{1s}+\omega-\omega_1)^2+\Gamma_{1s}^2/4^2}\delta(\omega_1-\omega_{2p_j}-\omega-\omega_2)d\omega$$
$$= A\frac{\omega_2}{\omega_1}\frac{(\omega_{1s}-\omega_{2p_j})g_{2p_j}(\omega_{1s}-\omega_{2p_j}+\omega_1-\omega_2)(dg_{1s}/d\omega)}{(\omega_{1s}-\omega_{2p_j}-\omega_2)^2+\Gamma_{1s}^2/4\hbar^2} \quad (3)$$

and the $dg_{1s}/d\omega$ is then given by

$$\frac{dg_{1s}}{d\omega} = \frac{1}{A}\frac{d\sigma(\omega_1)}{d\omega_2}\frac{\omega_1}{\omega_2}\frac{(\omega_{1s}-\omega_{2p_j}-\omega_2)^2+\Gamma_{1s}^2/4\hbar^2}{(\omega_{1s}-\omega_{2p_j})g_{2p_j}(\omega_{1s}-\omega_{2p_j}+\omega_1-\omega_2)}. \quad (4)$$

As the experimental x-ray RRS yield at the energy $\hbar\omega_2$ is proportional to the differential cross section $d\sigma(\omega_1)/d\omega_2$, the latter can be replaced in Eq. (4) by the measured Raman intensity. For a given beam energy ($\hbar\omega_1$) tuned below the $1s$ absorption edge, the profile of the distribution $dg_{1s}/d\omega$ can thus be derived from the corresponding x-ray RRS spectrum for a wide energy range ($\hbar\omega$). Actually, from Eq. (4) two profiles are obtained, that correspond to final vacancy states with $j=1/2$ and $j=3/2$, respectively. As only the sum of these two distributions is reflected in the experimental x-ray RRS spectrum, the obtained oscillator strength distribution is a sum of two profiles having similar shapes but shifted in energy. However, for the low-Z samples investigated in the present study, the shifts are only 0.3–0.6 eV [27] and therefore the resulting smearing of the total $dg_{1s}/d\omega$ distributions is small. On the other hand, in contrast to the absorption method, the obtained profile is not broadened by the atomic level width Γ_{1s} of the $1s$ state. Thus, if the experimental broadening is smaller than Γ_{1s}, more detailed $dg_{1s}/d\omega$ profiles can be obtained with this method than with absorption measurements [5].

IV. RESULTS AND DISCUSSION

A. Shape of the RRS x-ray spectra

The high-resolution x-ray RRS spectra measured for several beam energies tuned below the K absorption edges are depicted in Fig. 2 for Al and Al_2O_3 and in Fig. 3 for Si and SiO_2. The energy calibration of the monochromator was obtained by measuring the absorption spectra of the Al and Si samples in the fluorescence mode, assuming for the inflection points the energies of 1559.9 eV and 1840.1 eV reported in [27] for the K edges of these elements. The K edge energies of the two oxides were then deduced from the in-

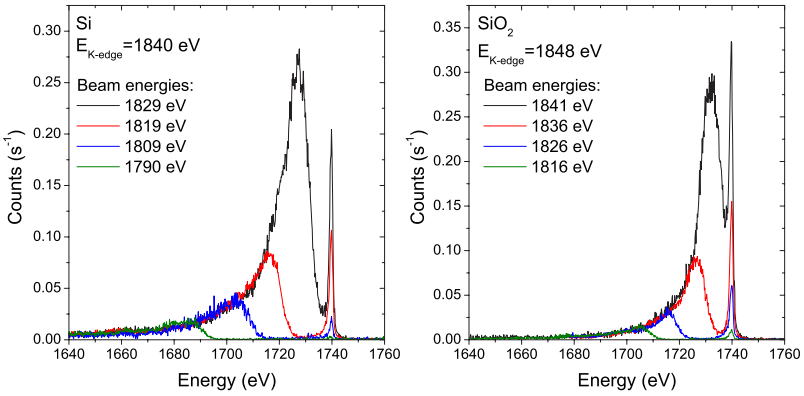

FIG. 3. (Color online) High-resolution x-ray RRS spectra of Si and SiO_2 measured for different beam energies tuned below the $1s$ absorption edge.

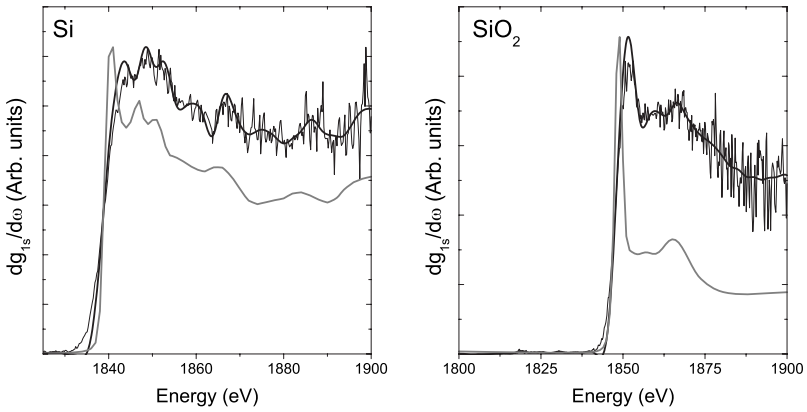

FIG. 4. Oscillator strength distributions obtained for Si and SiO_2 extracted from the corresponding RRS x-ray spectra (thin solid lines). The thick solid lines stand for the distributions that were obtained when a dedicated deconvolution procedure was applied (for details, see text). For comparison the corresponding absorption spectra [34] are also shown (gray lines).

flection points of the Al_2O_3 and SiO_2 absorption spectra. Energy shifts of +5.9 eV and +8.0 eV with respect to the parent elements were found for Al_2O_3 and SiO_2, respectively.

As shown in Figs. 2 and 3 each spectrum consists of two components: A broad structure corresponding to the RRS x-ray spectrum and a narrow line corresponding to the $K\alpha$ x-ray transition. The presence in the observed spectra of the $K\alpha$ x-ray line for beam energies tuned below the $1s$ edge is due to the high-energy tail of the monochromator response. For this reason, the intensity of this line for incident photon energies below the K edge diminishes rapidly and saturates above the absorption edge. The monochromator response was found to be well reproduced by a Gaussian with a FWHM of 6.1 eV and a small Lorentzian contribution (8%) with a FWHM of 10.0 eV accounting for the Lorentzian-like tails characterizing the multilayer monochromator profile.

In general the observed x-ray RRS structures have similar shapes as the ones predicted by theory. In particular, the maxima of the x-ray RRS spectra and the high energy cutoffs move with the beam energy according to the energy conservation law [see Eq. (2)]. One can also see that for all samples the tails in the low energy parts of the x-ray RRS structures merge together for any beam energy. This feature of the x-ray RRS spectra may be of practical interest for the TXRF technique. On the other hand, the experimental broadening results in a smearing of the observed spectra. For this reason, the high energy cut-off as well as the maximum of each RRS structure are significantly wider than those of the theoretical spectrum shown in Fig. 1.

B. Oscillator strength distribution $dg_{1s}/d\omega$

In order to extract more detailed information from the observed spectra data were analyzed using the Kramers-Heisenberg approach. First of all, a realistic $dg_{1s}/d\omega$ oscillator strength distribution was needed in order to fit properly the RRS spectra. As discussed in Sec. III, realistic $dg_{1s}/d\omega$ distributions can be extracted directly from the experimental x-ray RRS spectra. The method is explained in more detail below for the case of Si.

At first, the $dg_{1s}/d\omega$ function was determined using Eq. (4). The binding energies were taken from [27], the oscillator strengths g_{2p_j}, and the widths of the $1s$ and $2p$ states from [29,28], respectively. The energy range of the $dg_{1s}/d\omega$ function obtained in this way is limited by the energy domain covered by our measurements. The threshold is given by the cut-off of the emission spectrum and the high-energy limit by the lowest energy of the emitted photons. As a consequence, depending on the beam energy, the extension of the calculated $dg_{1s}/d\omega$ profiles varies. However, in the overlapping region (about 60 eV) the calculated profiles were found to be the same for each beam energy, as expected from theory, so that the average of these distributions was chosen for $dg_{1s}/d\omega$. For Si, this average distribution is presented in Fig. 4 (fluctuating thin solid line). In this figure the energy scale of the excited electrons ($\hbar\omega$) was transformed to the energy scale of the incoming photons ($\hbar\omega_1$) according to Eq. (2), assigning to the origin of the ($\hbar\omega$) scale the energy of 1840.1 eV reported in [27] for the $1s$ absorption edge. As shown, the obtained distribution has a similar shape as the spectrum measured by the absorption method but, due to the poorer statistics of the x-ray RRS measurements, the $dg_{1s}/d\omega$ distribution is more noisy. In addition, the observed differences in the spectral features at the edge, namely the shift of the first peak and the edge width, are due to the better beam energy resolution for the absorption spectra measurements. In order to diminish the noise and improve the resolution of the derived distribution, a more sophisticated method of analysis using a dedicated deconvolution procedure was developed.

Among existing spectral deconvolution techniques (see, e.g., [31–33]), the method proposed by Filipponi [32] was found to be the most appropriate one to deconvolve XAFS-like functions. Assuming that the measured profile $\widetilde{dg}_{1s}(E)/d\omega$ results from the convolution of the real $dg_{1s}/d\omega$ distribution with the experimental response function G, one can write

$$\frac{\widetilde{dg_{1s}}(E)}{d\omega} = \int \frac{dg_{1s}(E')}{d\omega} G(E-E')dE' . \qquad (5)$$

The easiest way to obtain the real function $dg_{1s}(E)/d\omega$ consists to use a deconvolution method based on the Fourier transformation. Within this method, the extracted profile and broadening function are first transformed into the Fourier space, then the first Fourier transform is divided by the second one and the result is finally transformed back into the energy space:

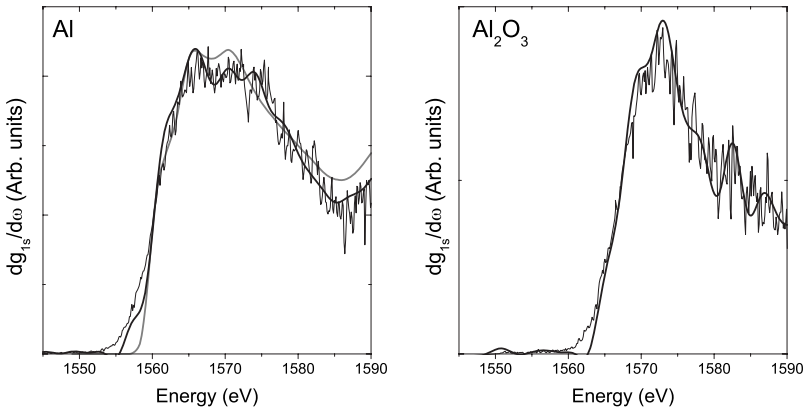

FIG. 5. Oscillator strength distributions obtained for Al and Al_2O_3 extracted from the corresponding RRS x-ray spectra (thin solid lines). The thick solid lines stand for the distributions that were obtained when a dedicated deconvolution procedure was applied (for details, see text). For comparison the absorption spectrum of Al reported in [35] is also shown (gray line).

$$\frac{dg_{1s}(E)}{d\omega} = \mathcal{F}^{-1}\left[\mathcal{F}\left[\frac{\widetilde{dg_{1s}}(E)}{d\omega}\right] \Big/ \widetilde{G}(q)\right], \tag{6}$$

where $q=2\pi/\hbar\omega$. In our experiment the broadening was mainly due to the beam energy distribution which could be represented approximately by a Gaussian with a standard deviation σ of about 2.6 eV. In the direct and Fourier spaces the Gaussian broadenings are given respectively by

$$G(E) = \frac{1}{\sqrt{2\pi\sigma^2}}\exp\left(-\frac{E^2}{2\sigma^2}\right), \tag{7}$$

$$\widetilde{G}(q) = \exp\left(\frac{-\sigma^2 q^2}{2}\right). \tag{8}$$

As in the Fourier transformation the noise blows up even for small values of σ, an additional filter was employed in the deconvolution process. The filter consisted to add a third power term in q in the argument of the $\widetilde{G}(q)$ function to prevent the latter to converge to zero for the $q\to\infty$ limit. With this filter the deconvolved $dg_{1s}/d\omega$ distribution is finally given by

$$\frac{dg_{1s}(E)}{d\omega} = \mathcal{F}^{-1}\left[\mathcal{F}\left[\frac{\widetilde{dg_{1s}}(E)}{d\omega}\right]\exp\left(\frac{\sigma^2 q^2}{2} - b(q-q_0)^3\right)\right], \tag{9}$$

where b is a constant and q_0 which is of the order of 0.3 eV^{-1} serves to enhance and sharpen the features present in the spectra [32]. When applying the Fourier transform a further difficulty resided in oscillations stemming from the steplike shape and the finite interval of our distribution. The problem was solved by subtracting a linear function from $\widetilde{dg_{1s}}/d\omega$ so that the first and last points of the distribution had the same value after the subtraction. The linear function was then simply added to the deconvolved distribution since, according to the Cauchy principle, the deconvolution of a linear function results in the same linear function. To check the reliability of the described deconvolution method, the latter was applied to functions resulting from the folding of known profiles. Quite satisfactory results were obtained for the deconvolved curves which were found to match rather well the original ones, neither artificial peaks nor oscillations being observed as a result of the deconvolution.

As the Fourier transform is a noise-sensitive process, raw data were smoothed before their deconvolution, using the Slavitzky-Golay filter. As it can be seen from Fig. 4, the noise level is not constant but grows with energy. Actually this is not surprising because the high-energy part of the $dg_{1s}/d\omega$ distribution corresponds to the low-energy part of the emission spectrum where the fluctuations are much bigger than in the near cutoff region. For this reason, before smoothing the data, a variable binning was employed in which the number of binned points was increased with energy, in order to bring the normalized sums of binned points to the same statistical error. However, to preserve the fine structures present in the spectrum, the energy range corresponding to the binned points was always kept smaller than the experimental resolution.

The result of the deconvolution of the previously smoothed $\widetilde{dg_{1s}}/d\omega$ distribution of Si is depicted in Fig. 4 (thick solid line). As shown a significant improvement is brought by the binning-smoothing procedure. For instance, the small structures around 1870 eV and 1885 eV are better resolved and in the near edge region a triplet structure appears which was hardly visible before.

The same deconvolution method was employed for SiO_2, Al, and Al_2O_3. Results are presented in Figs. 4 and Fig. 5, respectively. At first one sees that significant differences are observed between Al and Si, although the two elements differ only by one unit in the atomic number Z, as well as between the pure elements and their oxides. A further inspection of the two figures shows that for Si, SiO_2, and Al the overall shapes of the derived distributions are similar to those obtained by means of absorption measurements. For Al_2O_3, no comparison could be performed since no corresponding XANES (near edge x-ray absorption spectroscopy) spectrum for an amorphous sample was found.

In the case of Si, the triplet structure appearing around 1842 eV reflects the density of states of the conduction band [36] while the structures at 1862 eV and 1883 eV are due to the multiple scattering effects reported in [37]. A similar triplet structure is observed in the near edge region of SiO_2 in good accordance with the absorption spectra reported in [34,36,38]. The strong white line around 1850 eV, which is less sharp and shifted to higher energies in our case as a result of the poorer beam energy resolution, has been assigned in [36] to an excitonic state with p symmetry. Regarding Al, the near edge structure can be interpreted in terms of

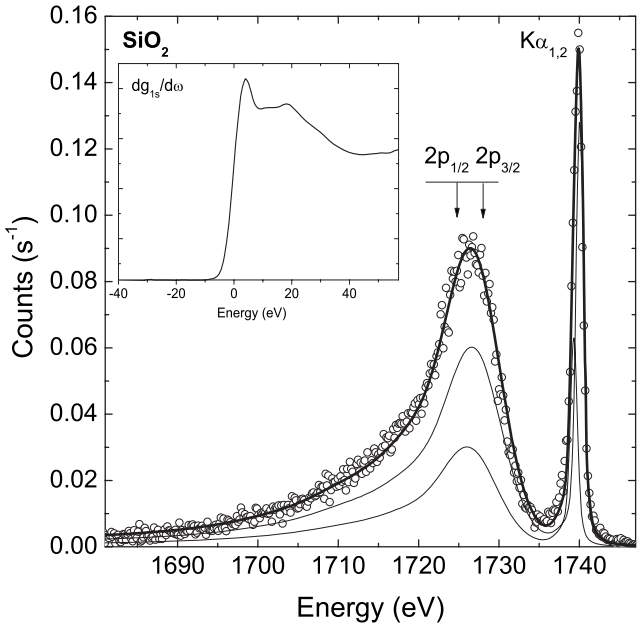

FIG. 6. Theoretical shape of the x-ray RRS spectrum of SiO_2 calculated for an excitation energy of 1836 eV (thick solid line). Thin lines correspond to final states with the vacancy in the L_2 and L_3 subshells. The open circles represent the experimental spectrum. The oscillator strength distribution used in the calculations is shown in the inset.

unoccupied levels with a majority contribution of p and d states as discussed in [35].

Here, we would like to point out that the possibility to obtain XAFS-like information over a wide energy range from x-ray RRS spectra has not been demonstrated experimentally beforehand, probably because of the extremely low x-ray RRS cross sections. In fact, as shown in the present paper, x-ray RRS measurements can represent an alternative to absorption measurements for studying the electronic properties in materials.

C. Shape of the x-ray RRS spectra vs Kramers-Heisenberg formalism

The $dg_{1s}/d\omega$ distributions derived with the method described in the preceding section can now be employed to calculate the shapes of the x-ray RRS spectra using the Kramers-Heisenberg formula. An example of the results obtained from these numerical calculations is shown for SiO_2 in Fig. 6.

The energies of the $1s$ and $2p$ levels of SiO_2, which are needed in the calculations, were derived directly from the experiment. At first, the energy of the $1s$ level was determined from the inflection point of the K-absorption edge measurement. A value of 1848.1 eV was found. The energies of the two $2p$ levels were then determined by subtracting from the above value the fitted energies of the $K\alpha_{1,2}$ doublet measured in the off-resonance regime. Results of 108.1 eV and 107.5 eV were obtained for the $2p_{1/2}$ and $2p_{3/2}$ levels, respectively. The fitted Lorentzian widths of the $K\alpha_1$ and $K\alpha_2$ lines were found to be the same as those obtained in the fit of elemental Si, so that the widths Γ_{1s} and Γ_{2p} and the oscillator strength g_{2p_j} occurring also in the Kramers-Heisenberg formula were assumed to be the same as those reported for Si in [28,29].

The x-ray RRS profile calculated by means of Eq. (1) as well as the fluorescence $K\alpha$ line were then fitted to the data. As shown in Fig. 6 a quite satisfactory agreement was achieved. Similar good agreements between the shapes of the experimental and theoretically computed spectra were observed for the other samples and any employed beam energy. Note that for a given sample the theoretical x-ray RRS yield was scaled to match the experimental intensity but the same scaling factor was then used for the x-ray RRS spectra taken at different energies. It can be concluded that the shapes of x-ray RRS spectra can be well reproduced by the Kramers-Heisenberg approach, using the Tulkki and Åberg formula. However, we have found that good fits to the experimental data were only obtained when the proper $dg_{1s}/d\omega$ distribution was used in the calculations. This is probably not true for low-resolution ($\Gamma_{exp} > 100$ eV) TXRF measurements, for which precise enough theoretical x-ray RRS spectra can be computed using a simple step function for the $dg_{1s}/d\omega$ distribution.

D. X-ray RRS cross sections

The total cross sections for the x-ray RRS process were derived from the experimental intensities of the integrated x-ray RRS spectra normalized to the intensity of the parent $K\alpha$ x-ray lines measured at beam energies about 50 eV above the $1s$ thresholds. Assuming that the x-ray RRS cross section for photon energies slightly below the K-edge is isotropic [23], the following relation was employed:

$$\sigma_{\mathrm{RRS}} = \frac{I_{\mathrm{RRS}}}{I_{K\alpha}} \sigma_K \omega_{K\alpha}, \tag{10}$$

where I_{RRS} and $I_{K\alpha}$ correspond to the integrated yields of the x-ray RRS spectra and $K\alpha$ transitions. The single K shell photoionization cross sections σ_K and the partial fluorescence yields $\omega_{K\alpha}$ were taken from [39,40], respectively. All x-ray yields were corrected for the differences in the absorption in the target of the incoming and outgoing photons, whereas the efficiency of the crystal spectrometer was assumed to be constant over the about 100 eV wide energy intervals covered by the present experiment.

The energy range of the x-rays emitted in the RRS process extends down to 0 eV, whereas only photons with energies bigger than the lower limits (E_{min}) of the measured energy intervals were observed. The value of E_{min} was 1400 eV for Al and Al_2O_3 and 1640 eV for Si and SiO_2. The problem was solved by extending the calculations of the theoretical x-ray RRS profiles down to 0 eV and by integrating then the theoretical spectra from zero to E_{min}. The so-obtained theoretical yields were then simply added to the measured x-ray RRS intensities to get the total x-ray RRS yields employed in the cross section determination. Since the shapes of the experimental x-ray RRS spectra were found to be very well reproduced by theory over the whole photon energy intervals covered by the measurements, one can ex-

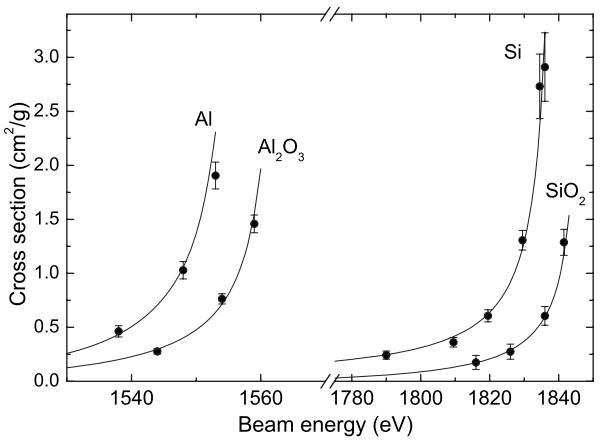

FIG. 7. Total x-ray RRS cross sections plotted versus the photon beam energies. The solid lines represent the corresponding theoretical cross sections computed by means of the Kramers-Heisenberg formula.

pect that the corrections for the missing experimental x-ray RRS yields obtained this way are reliable. Furthermore, as the low energy tails of the x-ray RRS spectra merge together below the maxima of the spectra (see Fig. 2 and Fig. 3), for a given sample the correction should be the same for any beam energy. This was confirmed by the calculations within the statistical uncertainties so that the same average yield correction was applied to all x-ray RRS spectra corresponding to the same target.

The total x-ray RRS cross sections obtained in the present work are presented in Fig. 7 for the four samples. The cross sections corresponding to the missing experimental x-ray RRS yields discussed above amount to 0.166 cm^2/g and 0.125 cm^2/g for Al and Al_2O_3, respectively to 0.123 cm^2/g and 0.072 cm^2/g for Si and SiO_2. The solid lines in Fig. 7 correspond to theoretical predictions based on the Kramers-Heisenberg formula. They were calculated by integrating Eq. (1) over the whole energy range of the emitted photons, i.e. from $\hbar\omega_2=0$ to $\hbar\omega_2=E_{cut\text{-}off}$. The constants A occurring in Eq. (1) were determined by fitting the theoretical cross section curves to the experimental points. As showed by the figure the beam energy dependency of the theoretical cross sections is in good agreement with the experimental data.

Because the 1*s* absorption edges lie 6 eV (Al_2O_3), respectively 8 eV (SiO_2), higher than those of the corresponding pure elements, the cross section curves of the oxides are shifted towards higher beam energies. Furthermore, a careful inspection of Fig. 7 shows that for the same energy differences with respect to the *K* edges, the x-ray RRS cross sections of the compounds are smaller by about a factor 2. This is due to the fact that the cross sections presented in the figure are expressed in cm^2/g and the number of Al or Si atoms per mass unit is about 2 times smaller in the oxides than in the pure elements (1.88 times smaller for Al_2O_3 and 2.14 for SiO_2). Converting in barns per atom the cross sections obtained for instance at beam energies 10 eV below the *K*-edges, one finds values of 61.8 b/atom and 75.5 b/atom for Al and Al_2O_3, and of 60.5 b/atom and 71.5 b/atom for Si and SiO_2. Approximately the same ratios $(RRS)_{oxide}/(RRS)_{element} \cong 1.2$ are obtained for other excitation energies. It seems therefore that the x-ray RRS cross sections of Al and Si are about 20% bigger in the oxides than in the pure elements when expressed in barns per atom. This is, however, not really unexpected, the unoccupied states above the Fermi level involved in the x-ray RRS process being affected by the chemical environment.

Other experimental data concerning x-ray RRS cross sections are very scarce and exist only for elemental Si [41–43]. Available data were determined by means of different techniques employing low-resolution detectors. Results reported in [41,42] were obtained using the $K\alpha$ x-rays of Si as incoming photons (1740 eV). Cross sections of $(58\pm20)\ r_0^2$ [41] and $(67\pm8)\ r_0^2$ [42] (where r_0 stands for the classical electron radius) were found. To compare our Si results to these former data, the curve corresponding to the least-squares fit to present Si cross sections was extrapolated to 1740 eV. A value of 0.116 ± 0.013 cm^2/g, i.e., $(68.1\pm7.7)\ r_0^2$ was obtained in good agreement with the above-mentioned experimental results and with the theoretical value of 61 r_0^2 reported by Åberg and Tulkki [23].

Very recently, a new set of experimental Si x-ray RRS differential cross sections was published [43]. The cross sections were determined for a wide energy range of incident photons (1580–1822 eV). The Si target was irradiated with monochromatized synchrotron radiation (resolving power of about 1000) and the scattered radiation was measured with a Si(Li) detector. From the curve reported in Fig. 6 of this paper, differential cross sections of $(5.1\pm0.4)\ r_0^2\ sr^{-1}$, $(14.4\pm1.0)\ r_0^2\ sr^{-1}$ and $(46.9\pm3.3)\ r_0^2\ sr^{-1}$ corresponding to beam energies of 1740 eV, 1800 eV and 1825 eV were deduced. Using the values of the least squares fit to our results corresponding to the three energies and transforming them into the same units, differential cross sections of $(5.4\pm0.6)\ r_0^2\ sr^{-1}$, $(14.5\pm1.4)\ r_0^2\ sr^{-1}$ and $(41.6\pm3.7)\ r_0^2\ sr^{-1}$ are found that are again consistent within the combined errors with the ones from [43]. However, for beam energies close to the 1*s* edge (e.g., the third chosen energy in the above comparison), the results reported in [43] seem to be somewhat bigger than ours. A plausible explanation for the deviations, if any, may reside in some contamination of the x-ray RRS spectra of [43] by the fluorescence $K\alpha$ line of Si. At beam energies close to the 1*s* threshold, the $K\alpha$ line can indeed be induced by photons from the high-energy tail of the beam energy distribution, leading to some excess of intensity in the x-ray RRS spectra since $K\alpha$ x-rays cannot be separated from high-energy x-ray RRS photons in low-resolution measurements.

E. Measurements across the 1*s* absorption edge for Al and Si

For Al and Si, the measurements were extended to beam energies tuned across the *K* edge. The corresponding x-ray RRS spectra are presented in Fig. 8 and Fig. 9. From the two figures, the evolution of the target x-ray emission from the fluorescence $K\alpha$ emission to the x-ray RRS emission while the beam energy is tuned across the edge is clearly visible. As also shown by the figures, the overall x-ray emission

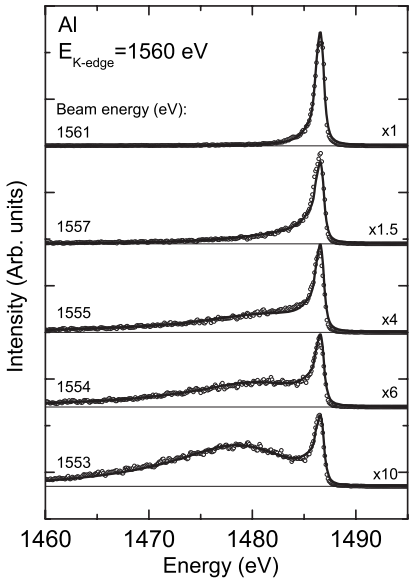

FIG. 8. High-resolution RRS x-ray spectra of Al for incident beam energies tuned across the 1s absorption edge. The open circles represent the experimental spectra, the solid lines the theoretical predictions calculated with the Kramers-Heisenberg formula for continuum excitations. For comparison with the yields of the x-ray RRS spectra depicted in Fig. 2 the spectrum measured at 1553 eV is shown again.

yields diminish drastically with the beam energy as soon as the latter is tuned below the 1s edges.

Measurements in the near edge region are interesting because they permit to probe the goodness of calculations in the energy region corresponding to the $\hbar\omega_1 \rightarrow \hbar\omega_{1s}$ limit,

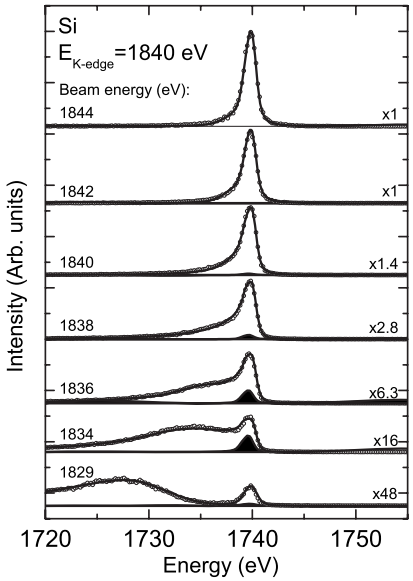

FIG. 9. High-resolution RRS x-ray spectra of Si for incident beam energies tuned across the 1s absorption edge. The open circles represent the experimental spectra, the solid lines the theoretical predictions comprising both the continuum and discrete excitations, and the filled areas the discrete 1s-3p excitation. For comparison with the yields of the x-ray RRS spectra depicted in Fig. 3 the spectrum measured at 1829 eV is shown again.

where there is a transition from the x-ray RRS process towards characteristic fluorescence. On the other hand, when the beam energy is tuned close to the absorption threshold one can hope to observe excitations to discrete unoccupied levels. From the experimental point of view, however, measurements across the 1s edge are difficult because the absorption of the beam in the target varies rapidly. Very careful beam energy dependent corrections for the intensity attenuation of the incoming photons in the target were necessary to obtain reliable results. This point was crucial for the present experiment since thick targets were employed.

To reproduce the evolving shape of the x-ray emission spectra observed in the near edge region, each spectrum was considered as the sum of a x-ray RRS profile and a 2p-1s transition. The x-ray RRS profiles of the two samples were determined by means of the Tullki and Åberg formula using the oscillator strength distributions determined from the spectra measured below the edges (see Sec. IV B). For each sample, all x-ray RRS profiles were normalized in intensity with the same scaling constant. The shapes and positions of the Al and Si $K\alpha$ lines were kept constant in the calculations, using the centroid energies and widths obtained from the fits of the lines measured 50 eV above the edges. The variation of the intensity of the $K\alpha$ line across the edge was computed using the intensity measured above the edge and correcting it by the relative number of incident photons having an energy bigger than the 1s threshold. As for each measurement the position and shape of the beam energy profile (area normalized to 1) were known, the fraction of incoming photons having enough energy to produce a 1s photoionization was determined by integrating the beam profile, using as lower integration limit the 1s threshold energy.

Results of these calculations are shown in Figs. 8 and 9 (thick solid lines). From Fig. 8 one sees that for aluminium the experimental spectra are well reproduced by the calculations. In the case of silicon, some discrepancies between theory and experiment were observed for beam energies tuned slightly below the 1s absorption edge, the calculated intensities of the $K\alpha$ line being systematically lower than the measured ones. These deviations which were found to vary with the beam energy, the maximum being observed at 1836 eV, suggested the existence of additional, beam energy dependent, 1s-np photoexcitations that were not considered in the calculations. Further calculations were thus performed, using the generalized Kramers-Heisenberg formalism which allows the inclusion of discrete excitations, by assuming $dg_{1s}/d\omega = g_{1snp}\delta(\omega_{np}+\omega)$ in Eq. (1) [23]. Within this formalism, the line shape of the 1s-np photoexcitation can by described by the following equation [22,23]:

$$\frac{d\sigma_{np}(\omega_1)}{d\omega_2} = A\frac{\omega_2}{\omega_1}\frac{(\omega_{1s}-\omega_{2p_j})g_{2p_j}(\omega_{1s}-\omega_{np})g_{1snp}}{(\omega_{1s}-\omega_{np}-\omega_1)^2+\Gamma_{1s}^2/4\hbar^2} \times \frac{\Gamma_{2p_j}/2\hbar}{(\omega_1-\omega_{2p_j}+\omega_{np}-\omega_2)^2+\Gamma_{2p_j}^2/4\hbar^2}. \quad (11)$$

The most probable 1s-np photoexcitation in silicon corresponds to $n=3$. The 3p levels are valence band states with binding energies between 0 and 5 eV. This energy interval is

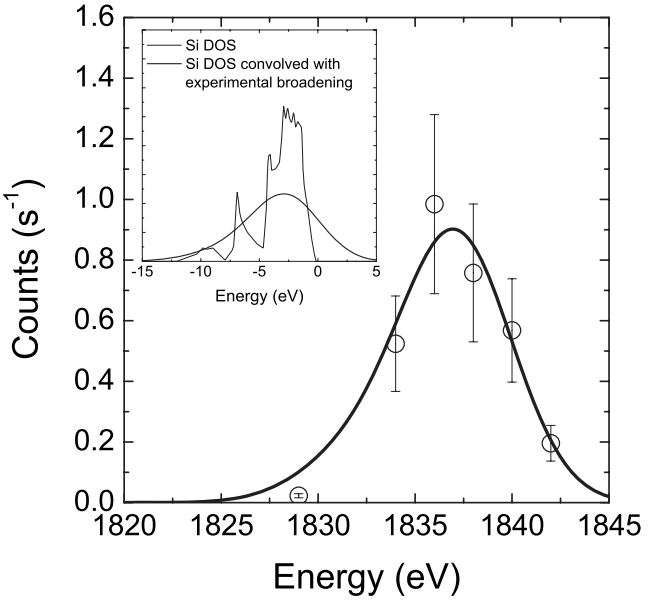

FIG. 10. Measured intensity evolution of the Si 1*s*-3*p* excitation (open circles). The thick solid line represents the fit to the data of the convolved DOS function. The DOS profile of the Si 3*p* states is depicted in the inset (thin solid line) as well as the convolution of this profile with the experimental response function (thick solid line).

consistent with the energy difference between the 1*s* threshold (1840 eV) and the energy for which the biggest intensity deviation was observed (1836 eV). Actually, assuming that the intensity deviations between theory and experiment are due to the 1*s*-3*p* excitation, the variation of the deviations as a function of the beam energy corresponds to the evolution with energy of the 1*s*-3*p* photoexcitation. This evolution is depicted in Fig. 10 (open circles). In the inset of Fig. 10 results of density of states (DOS) calculations for the 3*p* states of Si taken from [44] are presented (thin solid line). Convolving the DOS distribution with the known experimental broadening results in the curve represented in the inset by the thick solid line. The convolved curve was then fitted to the observed intensity deviations, using the curve centroid position and the area as free fitting parameters. The best fit result is represented by the thick solid line in Fig. 10. The weighted average position given by the fit is 1836.4 eV. Since the *K*-edge energy of Si was determined to be 1840.1 eV, an average binding energy of −3.7 eV is found for the 3*p* level, in fair agreement with the weighted average value deduced from the DOS calculations (−3.5 eV).

A third term corresponding to the 1*s*-3*p* excitation was thus added in the computation of the theoretical shapes of the Si spectra measured across the *K*-edge. As shown in Fig. 9, in which the 1*s*-3*p* excitation contributions are represented by filled areas, the experimental spectra are well reproduced by the calculations for all beam energies, included those around 1836 eV where significant deviations were observed before considering the 1*s*-3*p* excitation. At this point, we would like to point out that the 1*s*-3*p* photoexcitation in Si has not been observed before, neither in XANES spectra nor in XES measurements. This is most likely due to the weakness of the cross section for the 1*s*-3*p* excitation. The latter could be determined from our measurements. A value of 19.6±6.3 b/atom was found for incident photons of 1836.9 eV, a value which is about 7000 times weaker than the 1*s* photoionization cross section. For Al the 1*s*-3*p* excitation was not observed. This is, however, not unexpected since in metals the valence and conduction bands overlap, and because a high photon beam energy resolution is required to probe discrete excitations to unfilled upper levels.

V. SUMMARY

In conclusion, the x-ray RRS spectra of Al, Al_2O_3, Si, and SiO_2 were measured by means of high-resolution x-ray spectroscopy using monochromatized synchrotron radiation whose energy was tuned below and across the *K* absorption edges of Al and Si. The observed shapes of the x-ray RRS spectra could be well reproduced by calculations based on the Kramers-Heisenberg formalism, but only when realistic oscillator strength distributions were employed in the calculations. As predicted by theory the observed x-ray RRS spectra are characterized by high energy cutoffs and long low-energy tails. These tails merge together in the low energy range, no matter which beam energy is used. For all samples, the oscillator strength distributions could be extracted from the measurements. They were found to exhibit structures similar to those observed in absorption measurements. The total cross sections for the x-ray RRS process were determined as a function of the beam energy. The variation of the cross sections with the beam energy could be well reproduced by theory. For Si, the cross sections were compared to the few existing experimental and theoretical data. A quite satisfactory agreement was observed. Tuning the beam energy across the 1*s* absorption edge of silicon, we were able to observe the discrete 1*s*-3*p* excitation for the first time. The evolution of the excitation cross section with the beam energy was found to well reproduce the probability density of unoccupied 3*p* states predicted by DOS calculations.

ACKNOWLEDGMENTS

The authors would like to thank Dr. R. Tucoulou and his collaborators at the ESRF beam line ID21 for providing our experiment with very good beam conditions. They are also grateful to Dr. A. Mihelic from I.J.S., Ljubljana, for helpful discussions about the deconvolution problematics. The financial support of the Swiss National Science Foundation and the ESRF is acknowledged.

[1] A. Kotani and S. Shin, Rev. Mod. Phys. **73**, 203 (2001).
[2] A. Simionovici, J. P. Briand, P. Indelicato, and P. Chevallier, Phys. Rev. A **41**, 3707 (1990).
[3] C. Sparks, Phys. Rev. Lett. **33**, 262 (1974).
[4] P. Eisenberger, P. Platzman, and H. Winick, Phys. Rev. Lett. **36**, 623 (1976).
[5] H. Hayashi *et al.*, Phys. Rev. B **68**, 045122 (2003).
[6] M. Magnuson *et al.*, Phys. Rev. B **68**, 045119 (2003).
[7] G. Ghiringhelli *et al.*, Phys. Rev. Lett. **92**, 117406 (2004).
[8] S. M. Butorin *et al.*, Phys. Rev. Lett. **77**, 574 (1996).
[9] H. Hayashi *et al.*, Phys. Rev. B **70**, 155113 (2004).
[10] J. A. Carlisle *et al.*, Phys. Rev. Lett. **74**, 1234 (1995).
[11] J. A. Carlisle *et al.*, Phys. Rev. B **59**, 7433 (1999).
[12] A. Kikas *et al.*, Phys. Rev. B **70**, 085102 (2004).
[13] J.-E. Rubensson *et al.*, Phys. Rev. Lett. **64**, 1047 (1990).
[14] S. Shin *et al.*, Phys. Rev. B **53**, 15660 (1996).
[15] Y. Ma *et al.*, Phys. Rev. Lett. **74**, 478 (1995).
[16] S. Eisebitt *et al.*, J. Electron Spectrosc. Relat. Phenom. **93**, 245 (1998).
[17] D. Aswal *et al.*, J. Appl. Phys. **98**, 026103 (2005).
[18] R. French, J. Am. Chem. Soc. **73**, 447 (1990).
[19] R. Klockenkamper, *Total Reflection X-Ray Fluorescence Analysis* (Wiley, New York, 1997).
[20] K. Baur, J. Kerner, S. Brennan, A. Singh, and P. Pianetta, J. Appl. Phys. **88**, 4642 (2000).
[21] K. Baur, S. Brennan, B. Burrow, D. Werho, and P. Pianetta, Spectrochim. Acta, Part B **56B**, 2049 (2001).
[22] J. Tulkki and T. Åberg, J. Phys. B **15**, L435 (1982).
[23] T. Åberg and J. Tulkki, *Atomic Inner-Shell Physics* (Plenum Press, New York, 1985), pp. 419–463.
[24] F. Gel'mukhanov and H. Ågren, Phys. Rev. A **49**, 4378 (1994).
[25] J. Szlachetko *et al.*, Phys. Rev. Lett. **97**, 073001 (2006).
[26] J. Hoszowska *et al.*, Nucl. Instrum. Methods Phys. Res. A **376**, 129 (1996).
[27] R. D. Deslattes *et al.*, Rev. Mod. Phys. **75**, 35 (2003).
[28] J. L. Campbell and T. Papp, At. Data Nucl. Data Tables **77**, 1 (2001).
[29] J. H. Scofield, Phys. Rev. A **9**, 1041 (1974).
[30] H. Hayashi, Y. Udagawa, W. A. Caliebe, and C.-C. Kao, Phys. Rev. B **66**, 033105 (2002).
[31] P. K. Gupta, J. Phys. D **3**, 1919 (1970).
[32] A. Filipponi, J. Phys. B **33**, 2835 (2000).
[33] G. M. Petrov, J. Quant. Spectrosc. Radiat. Transf. **72**, 281 (2002).
[34] A. Owens, G. W. Fraser, and S. J. Gurman, Radiat. Phys. Chem. **65**, 109 (2002).
[35] E. Tamura, J. van Ek, M. Froba, and J. Wong, Phys. Rev. Lett. **74**, 4899 (1995).
[36] N. Nagashima *et al.*, Phys. Rev. B **48**, 18257 (1993).
[37] A. Bianconi *et al.*, Phys. Rev. B **36**, 6426 (1987).
[38] Y. Baba, T. A. Sasaki, and H. Yamamoto, Phys. Rev. B **49**, 709 (1994).
[39] http:/physics.nist. gov/xcom.
[40] F. B. Larkins, At. Data Nucl. Data Tables **20**, 313 (1977).
[41] J. M. Hall *et al.*, Phys. Rev. A **19**, 568 (1979).
[42] A. G. Karydas (private communication).
[43] M. Mueller, B. Beckhoff, G. Ulm, and B. Kanngieszer, Phys. Rev. A **74**, 012702 (2006).
[44] P. S. Fowles *et al.*, Phys. Rev. B **48**, 14142 (1993).